A Real-Time, Full-Duplex System for Underwater Wireless Optical Communication: Hardware Structure and Optical Link Model

JINJIA LI [1,2], **(Member, IEEE), BO YANG** [1], **(Member, IEEE), DEMAO YE** [3], **LINNING WANG** [1], **KANG FU** [1], **JINLONG PIAO** [1], **AND YONGJIN WANG** [1]
[1] Peter Grünberg Research Center, Nanjing University of Posts and Telecommunications, Nanjing 210003, China
[2] College of Rongcheng, Harbin University of Science and Technology, Weihai 264300, China
[3] 713th Research Institute, China Shipbuilding Industry Corporation, Zhengzhou 450015, China

Corresponding authors: Jinjia Li (2018010211@njupt.edu.cn) and Yongjin Wang (wangyj@njupt.edu.cn)

ABSTRACT Underwater wireless optical communication (UWOC) has been widely considered a supplement to traditional underwater acoustic communication. A real-time UWOC video delivery system was developed in a laboratory water tank based on a field-programmable gate array (FPGA) with binary frequency shift keying (2FSK) modulation. The system achieved full-duplex communication by using the transmission control protocol (TCP) and forward error correction (FEC). A high-power 445 nm light-emitting diode (LED) array was adopted to enhance the transmitted optical power and increase the transmission link distance. We present an underwater optical channel model that considers the effects of both geometry and channel loss, especially considering the impact of the refractive index of the optical medium and the non-line-of-sight (NLOS) links formed by water surface reflection. MATLAB was used to simulate this channel model and predict the received optical power distribution on the receiving plane. Additionally, we propose improved calculation methods for the consumed electrical power and transmitted optical power of the LED array. We also investigate the relationship between the optimum avalanche gain of an avalanche photodiode (APD) and the signal-to-noise ratio (SNR). This full-duplex system achieved a 1 Mbps data transmission rate at an SNR of 10.1 dB and a distance of 10 m for an underwater link. In addition, when the optical power of the LED array is enhanced, the link range is predicted to be 14.5 m with an attenuation coefficient of 0.056 /m.

INDEX TERMS Binary frequency shift keying, full-duplex, FPGA, high-power LED array, optical link model, Reed-Solomon code, underwater wireless optical communication.

I. INTRODUCTION

The ocean is the cradle of life. Approximately 71% of the Earth's surface is covered by the ocean. The vast marine resources on Earth are indispensable for many aspects of life. It is necessary to exploit and utilize those resources with underwater wireless communication (UWC) technology, which has considerable potential in facilitating the use of underwater vehicles, devices, observatories, and sensors. Underwater wired communication uses fiber optic or copper cable, which is expensive, inflexible, and vulnerable to marine life, making it largely infeasible for use in underwater mobile systems. Acoustic waves, radio frequency (RF) waves, and optical waves are three primary physical

The associate editor coordinating the review of this manuscript and approving it for publication was Xihua Zou.

information carriers for underwater wireless information transmission [1]–[3].

Acoustic waves involve mechanical waves with relatively little attenuation underwater (0.1-4 dB/km), and thus, they can cover long distances up to dozens of kilometers. However, acoustic waves have a low propagation speed (1500 m/s) and limited bandwidth (kHz), which leads to a multipath phenomenon, large time latency, and bulky antennas [2]. These characteristics hinder the application of acoustic waves in real-time and bandwidth-intensive scenarios. RF waves are another carrier that can provide a high data rate (Mbps), high bandwidth (MHz), and high speed of transmission underwater ($\approx 2.255 \times 10^8$ m/s). However, as the frequency increases, RF waves suffer from considerable attenuation due to the high conductivity of seawater (3.5-5 dB/m). This factor limits the transmission distance to only a few meters.

TABLE 1. The performance of some typical real-time experimental setups and commercial prototype UWOC systems.

Hardware/Prototypes	Light source/Photodetector	Modulation mode	Optical/electric power	Data rate	Link range	Mode	Ref.
Instrument	LD/APD	NRZ-OOK	19.4 mW	2.7 Gbps	34.5 m	Simplex	[9]
Instrument	LD/APD	8-PSK			1 m	Simplex	[10]
FPGA	LED/APD	OOK	250 mW (electric)	25 Mbps	10m	Simplex	[11]
FPGA	LD/PIN	16-QAM	60 mW	50 Mbps	3 m	Simplex	[12]
FPGA	LED/APN	PSK/QAM			25 m	Simplex	[13]
AquaOptical I	LED/APD	DPIM	500 mW	1.2 Mbps	30 m	Simplex	[14]
AquaOptical II	LED/APD	DPIM	10 W	2.28 Mbps	50 m	Simplex	[15]
Ambalux	LED/APD		36 W (electric)	10 Mbps	40 m	Simplex	[16]
Kaiko	LD/PMT		5 W	20 Mbps	120 m	Simplex	[17]
BlueComm 200	LED/PMT		6 W	10 Mbps	150 m	Simplex	[18]
FPGA	LD/PMT	NRZ-OOK	17 mW	1 Mbps	3.6 m	Simplex	[19]
Circuit	LED/LD/PD	GMSK	13.2, 38.4 mW	1 Mbps	3.6 m	Duplex	[20]
LightSpeed U15	LED/				7.6 m	Duplex	[21]
Circuit	LD/PIN	OOK		100 Mbps	1.6 m	Duplex	[22]
Circuit	LED/APD	NRZ-OOK		235 Mbps	11.5 m	Duplex	[23]
FPGA	LED/APD	2FSK	10.07 W	1 Mbps	14.5 m	Duplex	This work

Extremely low frequency (ELF) operation at 30-300 Hz is associated with low attenuation, and thus, these frequency bands are used for communication between submarines in military applications. It is worth noting that the attenuation coefficient of freshwater is frequency independent. Therefore, RF communication is a good choice in freshwater [2]. Nevertheless, any RF range requires a sizable antenna and high energy consumption. Light is a special electromagnetic wave with a large available bandwidth (THz), high speed of underwater transmission ($\approx 2.255 \times 10^8$ m/s), unprecedently high data rate (Gbps), and low latency. In addition, light-based UWC has low energy, low cost, and compact size advantages. The challenging underwater environment has a major impact on light transmission underwater. Absorption, scattering, and turbulence are dominant detrimental effects that degrade the optical transmission performance underwater. Fortunately, underwater optical wave transmission has a relatively low wavelength attenuation window. The 450-500 nm (blue-green) band has less attenuation for pure seawater or clear ocean water (0.4 dB/m) compared to other bands, and the 520-570 nm (yellow-green) band is suitable for coastal ocean or turbid harbor (11 dB/m) water types. Therefore, UWOC, also known as underwater visible light communication (UVLC), has become a feasible supplement or complementary solution to UWC, especially in short-range bandwidth-intensive applications [1], [3].

Typical applications of UWOC have appeared in recent years and attracted wide interest from industrial, scientific, and academic communities. Many studies have been performed on line-of-sight (LOS), diffused LOS, retroreflector-based LOS, and non-line-of-sight (NLOS) link configurations for UWOC. In addition, UWOC technology has been used to construct underwater wireless sensor networks (UWSWs) for optical communication with aerospace and terrestrial communication systems linked by autonomous underwater vehicles (AUV), remotely operated underwater vehicles (ROVs), communication buoys, and satellites. Even hybrid RF/acoustic/optical systems have been developed to increase the reliability of communication [1], [4].

Many studies of UWOC systems have been conducted from different perspectives, such as modulation schemes, coding techniques, experimental setups, and channel models. Some systems adopt offline processing models [5]–[8]; i.e., the transmitter uses an arbitrary waveform generator (AWG) or another instrument to generate a modulated optical signal, and the oscilloscope displays and stores the received data. The data is then processed with MATLAB on a computer. This offline mode is separated from the physical communication links, making these systems difficult to deploy on underwater vehicles. Real-time processing models typically have hardware structures for modulation, demodulation, and signal processing that can be conveniently applied in actual underwater environments. Due to their high design complexity, there are few commercial prototype UWOC systems that utilize real-time processing models. For example, AquaOptical series modems are prototype systems that were designed by MIT researchers [14], [15]. Additionally, Ambalux has released a commercial UWOC system with a data rate of 10 Mbps that operates over ranges up to 40 m [16]. In 2017, an underwater optical communication detector called "Kaiko" was designed and successfully achieved a 120 m link range and 20 Mbps data transmission rate [17]. In 2019, the BlueComm 200 series product was designed by Sonardyne, and it can achieve up to 150 m optical transmission at a rate of 10 Mbps [18].

Table 1 lists the performance of some typical real-time experimental setups and commercial prototype UWOC systems [14]–[18]. In [9] and [10], a real-time UWOC system based on instruments, e.g., an AWG and a signal quality analyzer, were developed. These UWOC systems were implemented with experimental instruments and had large volumes. However, field-programmable gate array (FPGA)-based UWOC systems are compact for practical application scenarios [11]–[13], [19].

Nevertheless, the systems mentioned above are all used for simplex communication, and duplex communication systems have seldom been reported. In [20]–[23], the ends of full-duplex and half-duplex systems were used as transceivers,
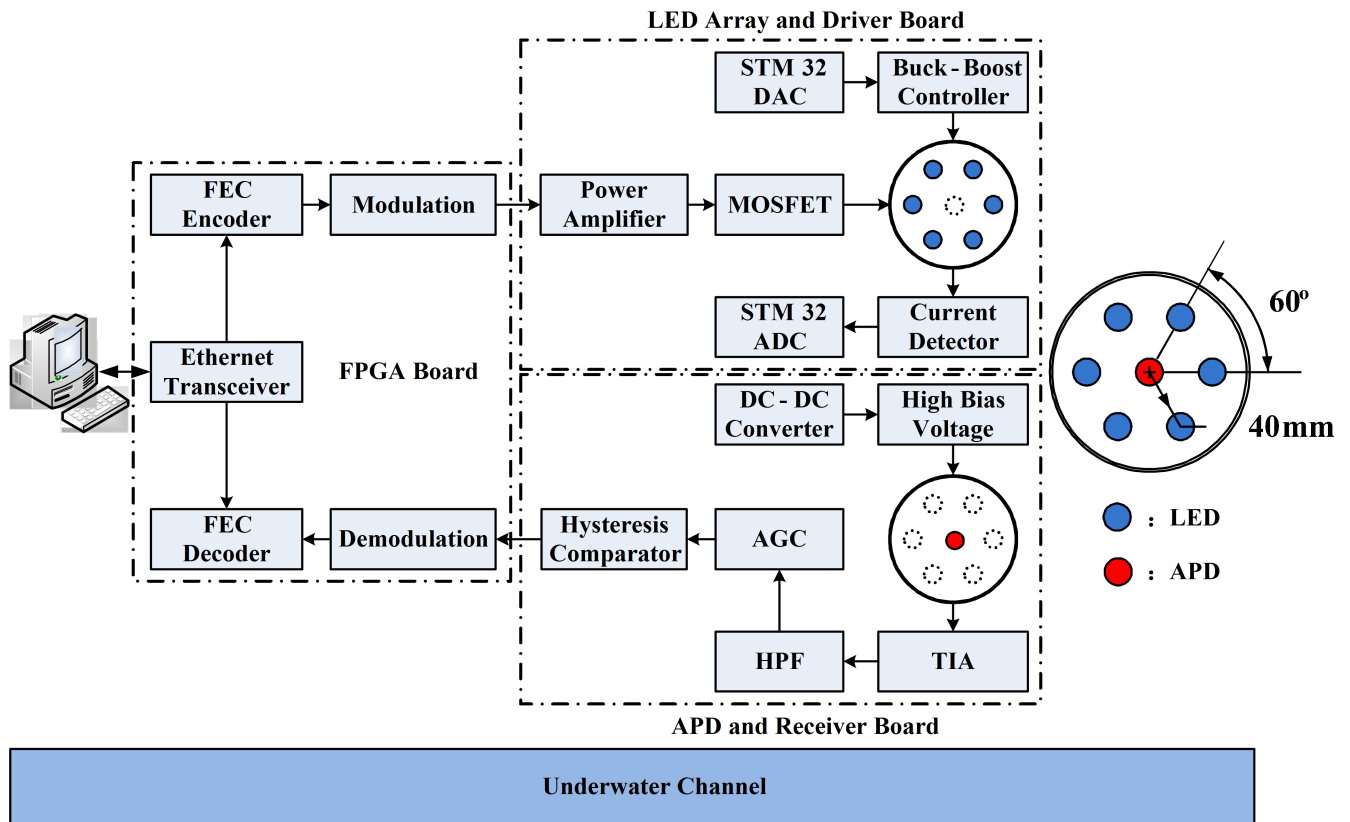
FIGURE 1. The hardware structure of the proposed UWOC system.

making these systems convenient for use in some applications, such as on ships or submarines and for diver and AUV to AUV communication [19]. Furthermore, in some cases, two sets of simplex systems have been used to form a duplex communication mode, such as AquaOptical II [15] and BlueComm 200. Unfortunately, duplex communication involves a self-interference phenomenon; i.e., the transmitted backscattered light is received by the co-located receiver. This self-interference phenomenon significantly reduces the signal-to-noise ratio (SNR) and is not conducive to long-distance link transmission. In [24], the backscattering disturbance in a duplex UWOC system was studied using a Monte Carlo model. If the transmitter and receiver in each terminal are close to each other, severe backscattering interference can occur.

In this paper, we experimentally demonstrate a real-time, full-duplex, point-to-point prototype UWOC system based on FPGA. The transmitting and receiving functions of each terminal are integrated for use as a transmitter or receiver. Through the high-power LED array, a 10 m link distance for duplex UWOC systems is achieved. We use the TCP, which has the disadvantage of a large delay but provides reliable data transmission. The reliable TCP for data transmission has important implications for some military applications. FEC Reed-Solomon (RS) codes are used to resist underwater channel fading. The remainder of this

paper is organized as follows. Section II describes the overall design of this system and the experimental setup. Section III introduces the experimental results and discussion. Finally, section IV concludes this paper.

II. SYSTEM OVERVIEW AND EXPERIMENTAL SETUP
The hardware structure of this real-time, full-duplex video transmission UWOC system is shown in Fig. 1. The structure consists of a PC information source and sink, an FPGA board, an LED array driver board, an APD receiver board, a power supply board, and an indoor water tank filled with tap water. Both terminals of the system have identical hardware structures that are symmetrical about the underwater channel. Fig. 1 only shows the hardware structure of one of the terminals.

A. FPGA AND CHANNEL CODING
The FPGA mainly completes ethernet data packet processing, channel coding, modulation, and demodulation tasks. The ethernet transceiver chip RTL8211EG (REALTEK) provides physical layer functions to transmit and receive ethernet data packets over unshielded twisted paired (UTP) cable. In order to improve the performance and mitigate the impact of attenuation and turbulence in the complex underwater channel, error-correcting coding (ECC) is widely applied in UWOC. ECC refers to added redundancy to the information sequence

to form a certain correlation relationship with the information bits so that the receiver not only detects errors but also corrects a limited number of errors in the received data sequence. Forward error correction (FEC) is one of the ECC modes without the use of feedback retransmission, and thus, it is suitable for real-time application scenarios. In the underwater fading channel, errors occur in sequences and bursts rather than randomly. The Reed-Solomon (RS) FEC codes are quite suitable for this channel with burst errors. In addition, RS code is robust and relatively simple [25], [26]. RS code is a type of non-binary Bose-Chaudhuri-Hocquenghem (BCH) code, which is defined by the Galois field GF (q). A q-ary RS (n, k) code can be expressed as

$$n = q - 1, q = 2^m, \quad m = 8$$
$$k = q - 1 - t$$
$$r = n - k = 2t \quad (1)$$

TABLE 2. RS code schemes employed in this system.

RS (n, k)	code rate k/n	check bytes r	error correction t
RS (255, 239)	0.94	16	8
RS (255, 223)	0.87	32	16
RS (255, 129)	0.51	126	63

where n is block byte of length, q is the number of GF elements, k is information bytes, r is redundant or check bytes, and t is the maximum number of bytes that can be error-corrected. In this work, the encoder maps n 8-bit information symbols onto 255 8-bit coded symbols, as shown in Table 2. The RS encoder is also completed by the cyclic code encoder, which is divided by the generator polynomial and can also be implemented with a shift register with feedback. The decoding method of the RS code is similar to the BCH code, except that the error position needs to be determined and then the error value can be calculated. Fig. 2 shows the software block diagram of RS code encoding and decoding based on FPGA, and the intelligent property (IP) core plays an important role in this process. The IP core is a macro module that has been repeatedly verified and has specific functions. In addition, the multi-layer coding scheme [10], [11] and convolutional codes can provide better performance. Low-density parity-check (LDPC) and Turbo codes are convolutional codes that close to the information theoretic limits, but they are more complicated.

TCP is a connection-oriented communication transport protocol that uses a multihandshake method to establish a reliable connection. When a packet is lost or the optical link is blocked, the system will request retransmission, which requires a transmission delay. Here, we construct a full-duplex optical transmission link based on TCP. The user datagram protocol (UDP) is another stream control protocol that does not require acknowledgement from the receiver, can be used for retransmission, and cannot recover lost packets. A performance comparison between TCP and UDP is shown in Table 3 [27]. A binary frequency shift keying (2FSK) [28]
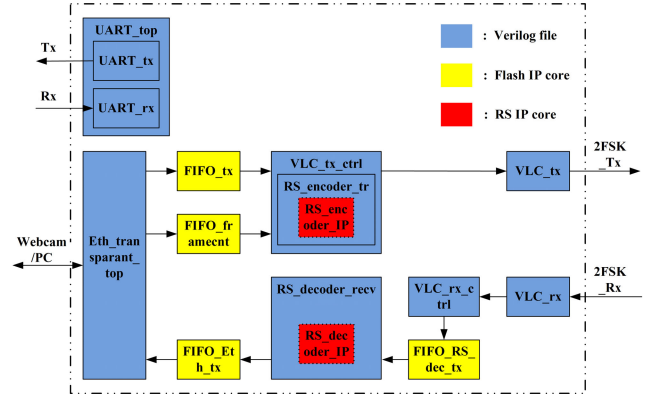

FIGURE 2. Software block diagram of RS code encoding and decoding based on FPGA.

TABLE 3. Performance comparison of TCP and UDP.

Metric	TCP	UDP
Communication mode	Duplex	Simplex
Reliability	High	Low
Delay	High	Low
Packet loss rate	Low	High
Fairness	Good	Bad

modulation scheme is used, a 1 MHz square wave indicates that data "1" has one carrier period, and a 2 MHz square wave indecates that data "0" has two carrier periods, as shown in Fig. 6.

B. HIGH-POWER LED ARRAY

In this novel array structure, six identical commercial high-power blue LEDs form a circular LED array as an optical source. The radius and angle are 40 mm and 60° for the LED array, respectively, and the specific structure is illustrated in Fig. 1. Six LEDs are connected in series and emit identical optical signals at the same time. The power rating of a single LED is 10 W, and that of an array is 60 W. The high-power array structure enhances the transmitted optical power and relaxes the pointing and alignment requirements [29]. Fig. 3 (a) shows the normalized electroluminescence (EL) spectra with different injection currents for this blue LED, and the center wavelength of emission is approximately 445 nm.
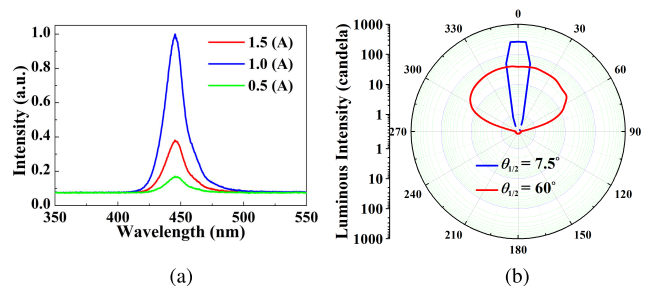

(a)

(b)

FIGURE 3. (a) The EL spectra of the LED (b) Luminous distribution of the LED.

This commercial LED has a power rating of 10 W and a half-beam angle of 60°. Due to the large divergence angle of the LED, the transmitted light energy is dispersed, which results in serious geometric losses. Therefore, it is necessary to design a secondary optical system to collimate the optical beam. A total internal reflection (TIR) lens arrangement is applied to collimate the optical beam as a parallel beam and enhance the optical intensity [30]. The LED is modeled with the Lambertian radiation model as

$$I(\theta) = I(0)cos^{m}(\theta) \tag{2}$$

$$m = -\frac{ln(2)}{ln(cos\theta_{1/2})} \tag{3}$$

where $I(\theta)$ is the luminous intensity at angle θ, $\theta_{1/2}$ is the semi-angle at half power, $I(0)$ is the center luminous intensity, and m is the order of Lambertian emission. As shown by the blue curve in Fig. 3 (b), the TIR lens decreases the semi-angle at half power from 60° to 7.5° and enhances the luminous intensity. The red curve in Fig. 3 (b) is the initial intensity distribution of the LED. High light intensity is beneficial for long-range transmission. High-power LEDs tend to have a smaller 3 dB bandwidth, as shown in Fig. 4.
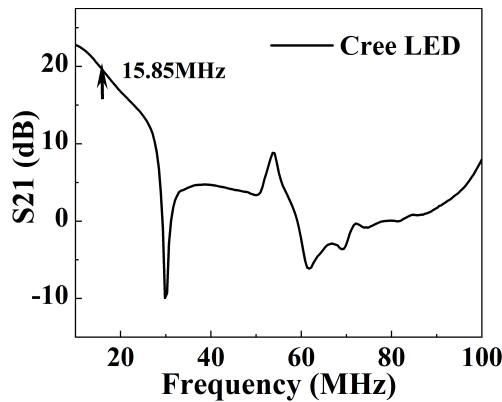

FIGURE 4. The 3 dB bandwidth of this high-power LED.

C. LED ARRAY DRIVER BOARD

The modulated signal is amplified by a wideband operational amplifier OPA2677 (Texas Instruments). We use the metal oxide semiconductor field-effect-transistor (MOSFET) model IPB042N03L (Infineon), which is characterized by very low on-resistance (max 4.2 mΩ), a drain source voltage (max 30 V), and a continuous drain current (max 70 A) to drive the LED array. To further improve the drive power, a MOSFET driver chip PDM2001D (NXP) is also required.

For optical communication systems, the stability of the brightness of the optical source is necessary. The brightness of an LED is mainly related to the amount of forward current. However, the current is temperature sensitive due to the negative temperature coefficient and exponential volt-ampere characteristics of LEDs. Here, an adaptive LED drive power with a boost-type DC-DC converter LTC3780 (Linear Technology) is introduced to supply stable current to the LEDs.
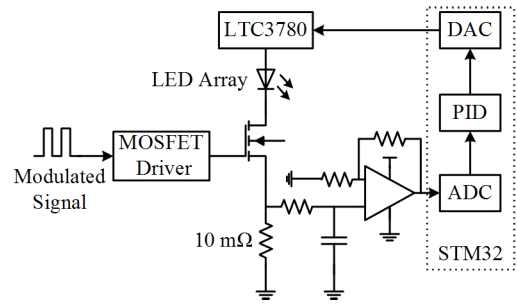

FIGURE 5. The LED closed-loop constant current drive circuit.

As shown in Fig. 5, the LED forward current can be calculated by the voltage drop of a precision resistor (10 mΩ). This voltage is filtered and amplified by the non-inverted amplifier and input into the analog-to-digital converter (ADC) of the microcomputer STM32F100C8T6 (STMicroelectronics). Proportional integral-derivative (PID) control is applied to achieve a stable and constant voltage, current, and LED array drive power. Fig. 6 shows the relationship between the 2FSK modulated signal and drain source or gate source voltage of MOSFET.
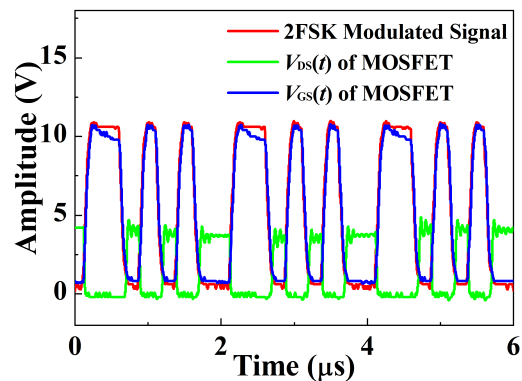

FIGURE 6. 1 MHz 2FSK modulated signal, drain source and gate source voltage of MOSFET. ("1" has one carrier period and "0" has two carrier periods).

## D. UNDERWATER CHANNEL MODEL

In this system, an indoor water tank is used to simulate an underwater channel, and the dimensions of the model are 10 m × 0.8 m × 0.8 m, as shown in Fig. 7 (a). An optical glass with a diameter of 300 mm is installed at both ends of the tank. This glass has a high transmittance in the visible light range, as shown in Fig. 7 (b). Fig. 7 (c) shows the tank filled with fresh tap water, and the attenuation coefficient is $0.056 \, m^{-1}$ [31]. The water tank walls were painted with black epoxy that had a relatively small reflective index.

Lots of UWOC systems have been tested using water tanks, but the effects of the refraction indices of different optical media have rarely been considered. As shown in Fig. 8, the optical beam transmits light through three optical media, i.e., air, optical glass, and water. Each refraction condition

(a)

(b)

(c)
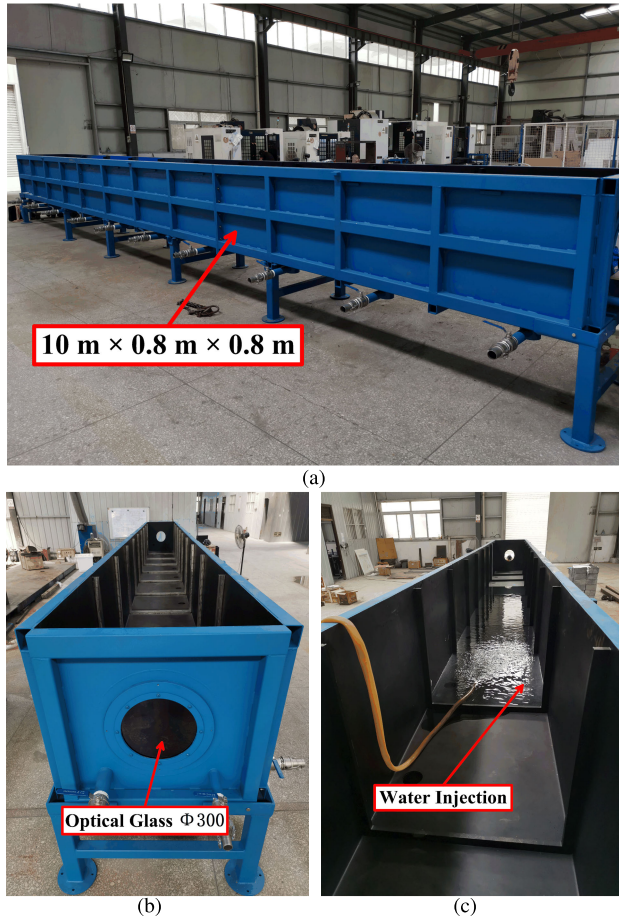
FIGURE 7. The indoor water tank. (a) Length, width, and height: 10 m × 0.8 m × 0.8 m. (b) Optical glass with a diameter of 300 mm. (c) Tap water injection and the tank walls painted with black epoxy. (This water tank was made by the 713th Research Institute of the CSIC).
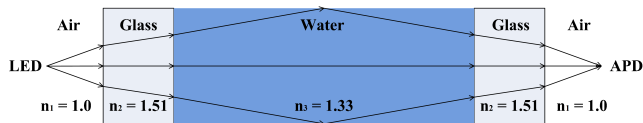
FIGURE 8. Refraction of the optical beam through three different optical media in the water tank.

will change the refraction angle of the beam [32]. The angle of refraction is based on Snell's law and given by

$$n_1 \sin\theta_1 = n_2 \sin\theta_2 \qquad (4)$$

where n_1 and n_2 is the refraction index and θ_1 and θ_2 are incident angle and refraction angle, respectively. We can calculate each refraction angle as shown in Table 4.

In this water tank underwater channel, the system forms a point-to-point communication configuration. If the optical beam is incident on the water surface, complete reflection will occur when the incident angle is greater than the water-air critical angle θ_c, which is calculated as

$$\theta_c = \arcsin\left(\frac{1}{1.33}\right) \approx 48.8° \qquad (5)$$

TABLE 4. The change in the refraction angle.

Optical media	Refractive index	Media interface	Refraction angle
Air	1.0	Air	$\pm 10°$
Optical glass	1.51	Air-optical glass	$\pm 6.58°$
Tap water	1.33	Optical glass-water	$\pm 7.49°$

where 1.0 and 1.33 are the refraction index values of air and tap water, respectively. Therefore, an NLOS optical link is also formed. However, the random water surface slope induced by the natural environmental may strongly disrupt the received signal in actual sea water [33]. Here, we assume that the water surface in the water tank is calm. The channel DC gain or geometric loss of the LOS and NLOS configurations are given as [34], [35]

$$H_{los}(0) = \frac{(m+1)A_{APD}}{2\pi d^2}\cos(\alpha)\cos^m(\beta)g(\alpha) \qquad (6)$$

where α denotes the incident angle, β is the angle of irradiance, d denotes the distance between the LED and APD, m is the order of Lambertian emission, A_{APD} is the APD effective active area, and $g(\alpha)$ is the gain of an optical concentrator.

$$H_{nls}(0) = \frac{(m+1)A_{APD}}{2(d_1 d_2)^2}\rho \cdot dA_{water} \cdot \cos^m(\beta)$$
$$\times \cos(\alpha_1)\cos(\beta_1)\cos(\alpha)g(\alpha) \qquad (7)$$

Here, α_1 is the angle of irradiance at a reflective point on the water surface, β_1 is the angle to the receiver at a given reflective point, d_1 denotes the distance between the transmitter and a reflective point on the water surface, d_2 denotes the distance between a reflective point and the receiver, dA_{water} represents small reflection elements, and ρ is the reflectivity coefficient. In accordance with Fresnel's law, the reflection coefficient is given by

$$R = \begin{cases} \frac{1}{2}\left[\frac{sin(\theta_i - \theta_t)}{sin(\theta_i + \theta_t)}\right]^2 + \frac{1}{2}\left[\frac{tan(\theta_t - \theta_i)}{tan(\theta_t + \theta_i)}\right]^2, & \theta_i < \theta_c \\ 1, & \theta_i \geq \theta_c \end{cases} \qquad (8)$$

where θ_i and θ_t denote the incident and reflected angles, respectively, and θ_c is the critical angle.

Channel modeling with UWOC is as complicated as that for free space optical (FSO) communication. The photons interact with water molecules, colored dissolved organic materials (CDOM), detritus, and phytoplankton, thus causing absorption and scattering phenomena. The absorbed photon energy is converted into heat or chemical energy, and the scattered photons can still be detected after multiple scattering events [2]. Turbulence and background noise are also factors that distort the optical signal. Real seawater channel models are mainly studied by Monte Carlo numerical simulations [36]. This laboratory water tank is filled with municipal water and has a low attenuation coefficient and a

limited scattering effect. The Beer-Lambert law is suitable for modeling such underwater channel loss and is given as

$$I(d) = I_0 \exp\left[-c(\lambda)d\right] \qquad (9)$$

where $c(\lambda)$ denotes the attenuation coefficient of water, d stands for the corresponding link range, I_0 is the initial transmitted optical power, and $I(d)$ is the received optical power at distance d from the transmitter. This law is accurate as long as the transmitter and receiver are well aligned and the water type has a low scattering coefficient. Finally, combining (6), (7), and (9), we can determine the received optical power as

$$P_{R-opt} = P_{T-opt} \exp\left[-c(\lambda)d\right]\left[H_{los}(0) + H_{nlos}(0)\right] \qquad (10)$$

where P_{T-opt} is the LED array transmitted optical power and P_{R-opt} is the received optical power.
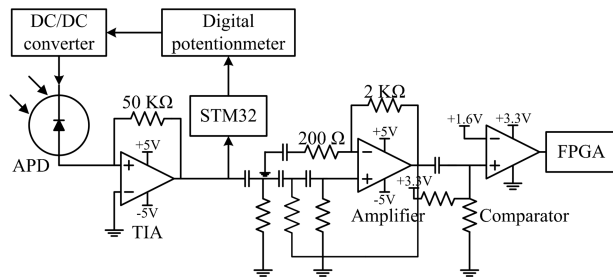

FIGURE 9. Schematic of the receiver circuit of the UWOC system.

E. APD AND RECEIVER BOARD

At the receiver side, a photodiode converts the attenuated and distorted weak light signals into current changes for optical-to-electrical conversion. The receiver adopts a short-wavelength-type silicon (Si) APD S8664-50K (Hamamatsu) with a 60 MHz cut-off frequency. The APD has a high internal gain and detection sensitivity, but it requires a very high breakdown bias voltage. Fig. 9 shows the circuit structure of the receiver. The transimpedance amplifier (TIA) converts the photocurrent from the APD into a voltage and passes it through a high-pass filter (HPF) to suppress the ambient noise associated with solar radiation and artificial illumination sources. After secondary amplification and digitization, the signal is output to the FPGA for demodulation. To maintain a stable amplification state in the TIA circuit, automatic gain control (AGC) is employed. An STM32 processor adjusts the resistance of the X9C103 (Xicor) digital potentiometer according to the real-time output voltage of the TIA, and the DC/DC converter is controlled to dynamically change the reverse bias voltage of the APD. The DC/DC converter adopts a HO1-P601-2C (MORNSUN) modem, which has a 0-600 V range that can be continuously linearly adjusted. Obviously, the dynamic range of light intensities at the receiver is increased by using an AGC strategy.

Responsivity describes the ability of the APD to convert incident optical power into photocurrent and can be
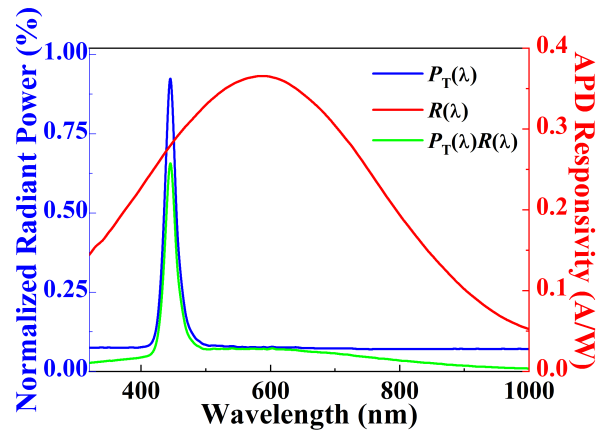

FIGURE 10. The normalized EL spectrum and the responsivity of APD.

calculated as

$$R(\lambda) = \frac{\lambda q \eta_{qe}}{hc} \approx \frac{\lambda(\mu m)}{1.24}\eta_{qe} \qquad (11)$$

Here, λ denotes the wavelength, q is the electronic charge, h is Planck's constant, c is the speed of light, and η_{qe} is the quantum efficiency. As shown by the red curve in Fig. 10, the responsivity of the APD is wavelength dependent. The blue curve in Fig. 10 is the EL spectrum of the LED. In general, the value corresponding to the center wavelength (445 nm) of the LED is used as the responsivity of APD, i.e., 0.28 A/W.

However, the responsivity values of the other wavelength components of the EL spectrum are not 0.28 A/W. Here, we calculate a more reasonable responsivity for the APD as

$$R(\lambda) = \frac{1}{P_T}\int_{320nm}^{1000nm} P_T(\lambda)R(\lambda)d\lambda \approx \frac{17.62}{70.45} \approx 0.25\,A/W \qquad (12)$$

where $P_T(\lambda)$ is the normalized EL spectrum, $R(\lambda)$ is the responsivity, the integral function $P_T(\lambda)R(\lambda)$ is shown by green curve in Fig. 10, 320 nm to 1000 nm is spectral response range of the APD, and P_T is the transmitted power obtained by integrating $P_T(\lambda)$, which is given as

$$P_T = \int_{320nm}^{1000nm} P_T(\lambda)d\lambda \qquad (13)$$

The calculated responsivity value is 0.25 A/W, which is approximately 0.03 A/W smaller than 0.28 A/W.

F. POWER SUPPLY MODULE

This UWOC system only requires an external DC +12 V power source. The PTN78000A (Texas Instruments) chip provides positive-to-negative voltage conversion, i.e., converts +12 V to −12 V. Then, ±12 V can be converted to ±5 V with a LM7805/7905 (National Semiconductor) chip. The HO1-P601-2C (MORNSUN) device has a +12 V input and a 0-600 V continuous linearly adjustable DC/DC converter. This output voltage can provide high reverse bias for the APD by adjusting the external digital potentiometer.
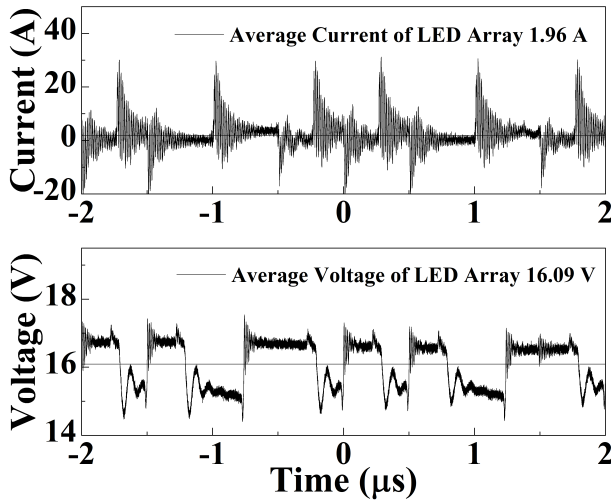
FIGURE 11. The average electric power (16.09 × 1.96 ≈ 31.5 W) consumed by the LED array.

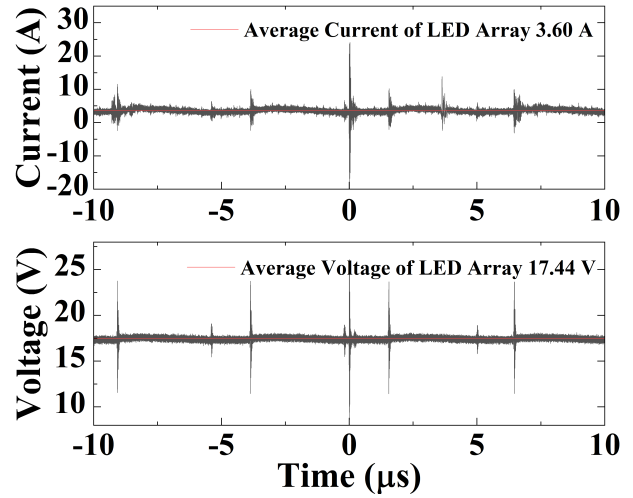**FIGURE 12.** The LED array consumes an average electric power (17.44 × 3.6 ≈ 62.8 W) on the MOSFET normally open state.

III. EXPERIMENTAL RESULTS AND DISCUSSION

A. CONSUMPTION OF ELECTRICAL POWER BY THE HIGH-POWER LED ARRAY

As shown in Fig. 5 and Fig. 6 above, the system uses a 50% duty cycle 2FSK modulated signal to drive MOSFET. The switching of the tube determines the transient change in the electrical power consumed by the LED array. In Fig. 11, we tested the transient voltage drop and current of the LED array and calculated the average voltage and current to obtain the average power consumed. The calculation of the current is derived from the 10 m? resistance voltage drop in Fig. 5. The LED consumes 31.5 W of electrical power on average, which is below the theoretical maximum of 60 W. If MOSFET is driven by a +12 V DC, the tube works in the normal open state and the LED works in the constant current state. Fig. 12 shows the average power (62.8 W) consumed in this state. Notably, the power in the normal open state is approximately twice that in the normal working state.

B. TRANSMITTED OPTICAL POWER

It is necessary to calculate the transmitted optical power of the LED array to determine the received optical power. Luminous flux is the radiant optical power that the human eye can perceive. However, the human eye has different sensitivities to light of different wavelengths, and the sensitivity can be determined by the relative visual function $V(\lambda)$, as shown in Fig. 13. Notably, the red curve reaches a maximum at 555 nm, and the blue curve is the normalized EL spectrum $P(\lambda)$, which is discussed above. The luminous flux can be calculated as [34]

$$683K \int_{380nm}^{780nm} P(\lambda)V(\lambda)d\lambda = P_E \cdot \eta_{lum} \qquad (14)$$

where K is the weighted coefficient of the *EL* spectrum, the constant 683 denotes the maximum luminous

TABLE 5. Some electro-optic parameters of the LED array.

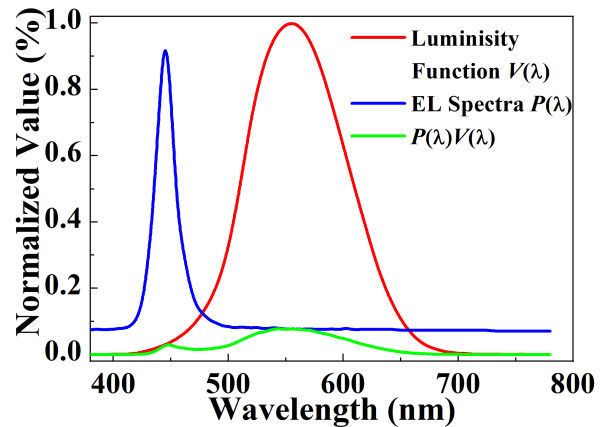| Metrics	Value
Average voltage (V)	16.1
Average current (A)	1.96
Average electric power (W)	31.56
Luminous efficiency (lm/W)	20.3
Luminous flux (lm)	639.45

FIGURE 13. Luminosity function and EL spectrum of the LED.

efficiency (lumens/W), η_{lum} is the LED luminous efficiency, and P_E is average electrical power of the LED array, which can be calculated from Fig. 11. The mean voltage and current values are listed in Table 5. The integrand function $P(\lambda)V(\lambda)$ is shown by the green curve in Fig. 13. In Table 5, the luminous efficiency is measured by an integrating sphere. Therefore, the luminous flux can be calculated as 639.45 lumens. Based on (14), we can obtain the weighted coefficient K as 0.14. The transmitted optical power spectral density (PSD) $KP(\lambda)$ is shown by the blue curve in Fig. 14 (a). As illustrated in Fig. 14 (a), the PSD is integrated to determine
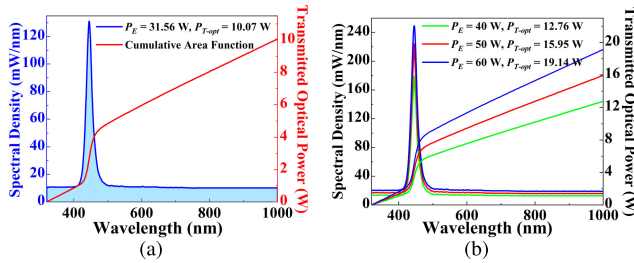
FIGURE 14. Integrate the optical PSD to obtain the transmitted optical power of the LED array.

the transmitted optical power, which is calculated as [35]

$$P_{T-opt} = K \int_{320nm}^{1000nm} P(\lambda)d\lambda \approx 10.07 \ W \tag{15}$$

where 320-1000 nm is the spectral response range of the APD. Therefore, the transmitted optical power of each LED is 855 mW. The electro-optical conversion efficiency of the LED is given as

$$\eta_{e-o} = \frac{P_{T-opt}}{P_E} = \frac{10.07W}{31.56W} \approx 31.9 \ \% \tag{16}$$

The same method is used to calculate the transmitted optical power, as shown in Fig. 14 (b). As the electrical power increases, the optical power becomes proportionally larger.

C. OPTICAL LINK MATLAB SIMULATION

Based on the abovementioned underwater channel model (10), we adopted a MATLAB simulation to model the underwater channel link and consider the parameters of the optical source, channel loss, geometric loss, and field of view (FOV) of the receiver, among others. The parameters required for the simulation are shown in the Table 6. The differences among indoor FSO link simulation methods are reflected in the attenuation coefficient of water and the effect of water surface reflection [37]. Fig. 15 shows the three-dimensional received optical power distribution on the receiver plane at different transmitted optical powers based on MATLAB simulations. Fig. 16 also shows the simulation results for the received optical power in dBm and μW.

TABLE 6. The parameters of underwater optical link MATLAB simulation.

Parameters	Value
Transmitted optical power of LED array	10.07, 12.76, 15.95, 19.14 W
Half power semi-angle of LED	7.5 deg.
The field of view of APD	70 deg.
APD effective active area	19.6 mm²
Tap water attenuation coefficient	0.056 m⁻¹
Tap water surface reflective index	0.8
Order of Lambertian emission	181.1
Length, width, and height of the water tank	10 m × 0.8 m × 0.8 m

D. RECEIVED OPTICAL POWER AND PERFORMANCE

The system transmitter is shown in Fig. 17, where the high-definition digital camera (HIKVISION) captures audio
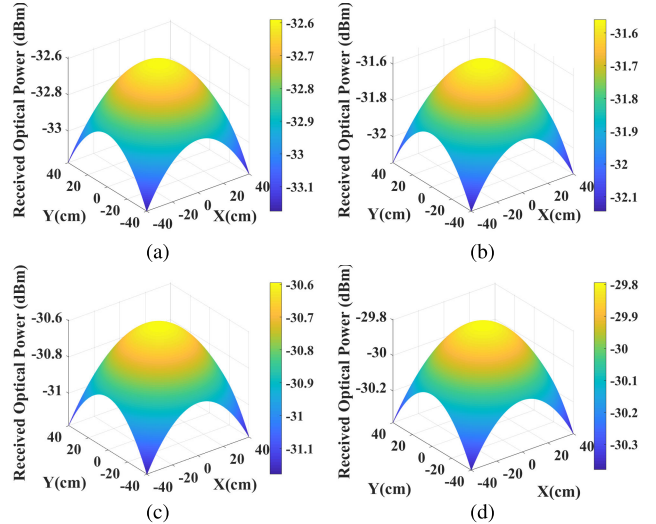

FIGURE 15. Received optical power distribution on the receiver plane at different average electric power P_E and transmitted optical power P_{T-opt} values. (a) $P_E = 31.6$ W and $P_{T-opt} = 10.07$ W. (b) $P_E = 40$ W and $P_{T-opt} = 12.76$ W. (c) $P_E = 50$ W and $P_{T-opt} = 15.95$ W. (d) $P_E = 60$ W and $P_{T-opt} = 19.14$ W.
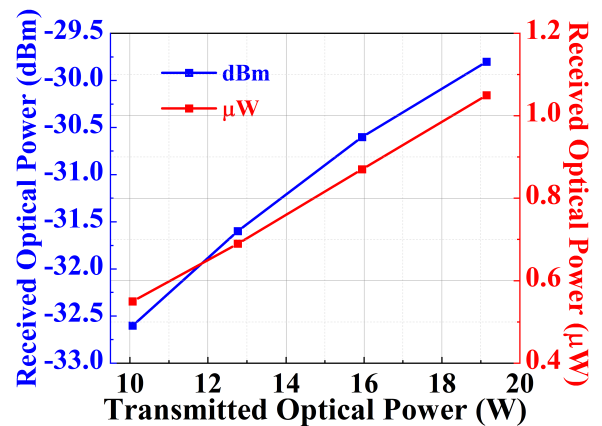

FIGURE 16. The received optical power of the APD at different transmitted optical powers.

and video images in real time. The video data are processed by the FPGA through the network port, and the LED array converts electrical signals to optical signals. The emitted light is transmitted through the 10 m underwater channel shown in Fig. 18. The attenuated and distorted optical signal is captured by the receiver shown in Fig. 19, and the computer displays the video image in real time.

Here, we assume that the transmitter and receiver are perfectly aligned. Then, the received optical power can be calculated as

$$P_{R-opt}(t) = \frac{V(t)}{R(\lambda)MR_L} \tag{17}$$

where $V(t)$ is the output voltage of the TIA, $R(\lambda)$ is the responsivity of the APD at $M = 1$, M is the avalanche multiplication factor of the APD, and R_L denotes the TIA load resistance. Here, the reverse voltage of the APD is 200 V,
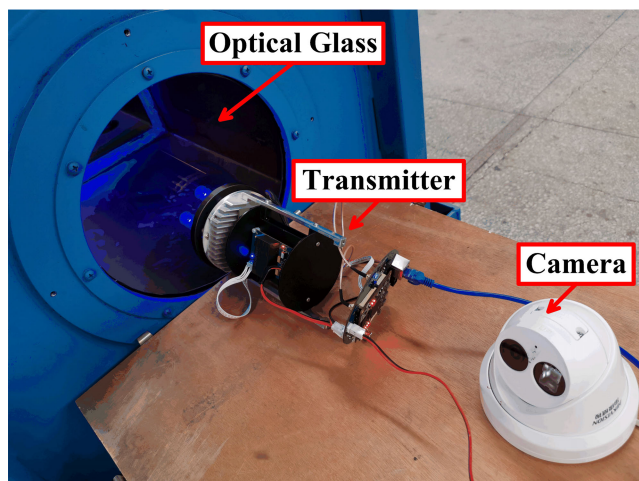
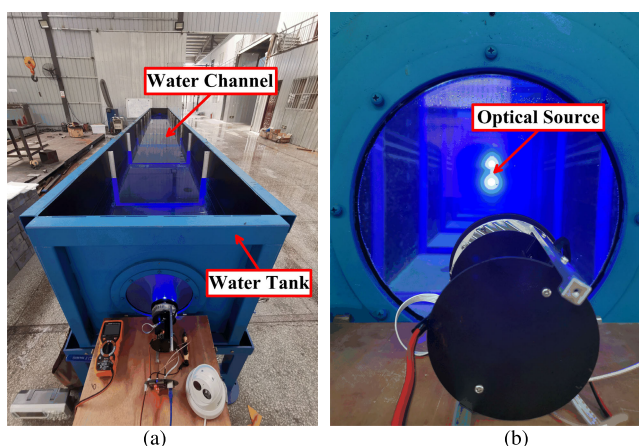**FIGURE 17.** The transmitter and digital camera for capturing video data.

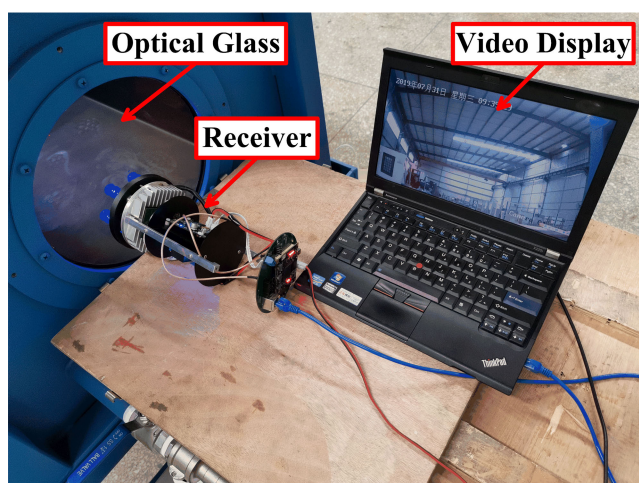**FIGURE 18.** 10 m underwater channel and indoor water tank.
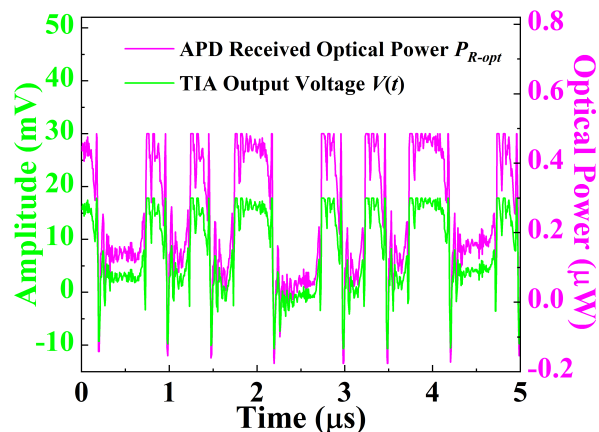

FIGURE 19. The receiver and video display.

FIGURE 20. TIA output voltage and received optical power.

alignment and the avalanche multiplication of the APD and configuration of the TIA circuit.
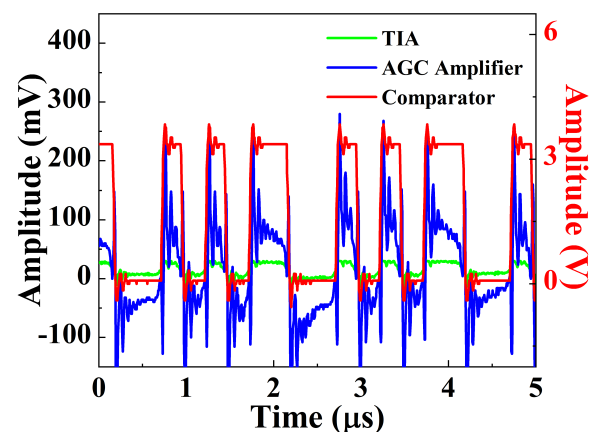
FIGURE 21. The output of the TIA, AGC amplifier, and comparator.
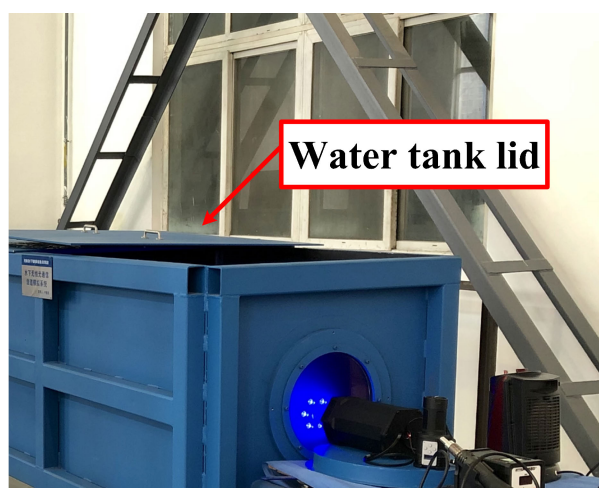
FIGURE 22. The water tank lid is used to reduce external light interference.

and M is taken as 2. As shown in Fig. 20, the average received power is approximately 0.32 μW, which is close to the MATLAB-simulated result of 0.54 μW shown as Fig. 16. The major cause of this deviation is the inaccuracy of link

Moreover, as shown in Fig. 21, the TIA output, AGC secondary amplifier output, and comparator digitized output waveforms were tested. In Fig. 22, we applied water tank lids

FIGURE 23. The 10 m FSO communication waveforms.

to reduce the external light interference during the day and night. Fig. 23 shows the case of 10 m FSO communication, and it is clear that a high light intensity is received. Obviously, FSO communication waveforms are smoother than underwater waveforms.
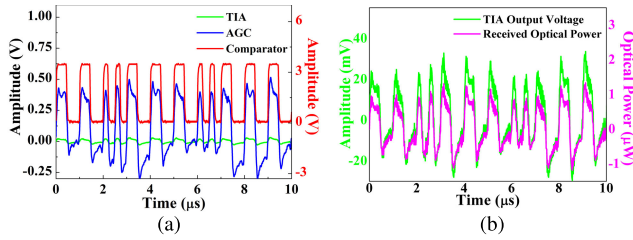
The above analysis and testing are based on the RS (255, 239) scheme. A stronger error correction scheme will further reduce the required optical power and improve the power efficiency but will simultaneously reduce the information rate. With the RS (255, 223) scheme, the system can receive optical power attenuated by neutral density filters with a transmittance of 90 %, and the RS (255, 129) scheme can receive 85 % attenuated light. However, the uncoded system does not work at 10 m. The required received optical powers at different RS code schemes are shown in Fig. 24 and Table 7.
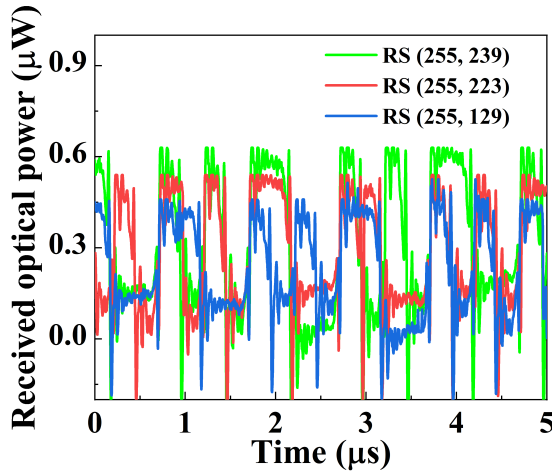

FIGURE 24. The required received optical power at different RS code schemes.

TABLE 7. The performance improvement by considering RS code.

RS (n, k) schemes	Received optical optical power dBm @ Matlab	Received average optical power μW
uncoded	-32.5	can not work
RS (255, 239)	-32.6	0.31
RS (255, 223)	-32.9	0.27
RS (255, 129)	-33.4	0.24

E. SIGNAL TO NOISE RATIO (SNR) AND SYMBOL ERROR RATE (SER)

The major noise sources of APD-based full-duplex UWOC systems are photocurrent shot noise, dark current noise,

and thermal noise. Moreover, duplex self-interference noise mainly arises from backscattering optical signals received by the co-located APD that are treated as background noise. The variance of these noise sources is given as

$$\sigma_{shot}^2 = 2qMF(M)(I_s + I_b + I_{self})B \quad (18)$$

$$\sigma_{dark}^2 = 2q(I_{ds} + M^2F(M)I_{db})B \quad (19)$$

$$\sigma_{thermal}^2 = \frac{4K_BTB}{R_L} \quad (20)$$

where q is the electron charge, M is the APD avalanche multiplication factor, $F(M)$ is the excess noise factor, and I_s and I_b are photocurrent not avalanched caused by useful signal and background light radiation, respectively. I_{self} is the self-interference photo-current, I_{ds} is the average surface leakage current, I_{db} is the average bulk leakage current, K_B is the Boltzmann constant, $T = 300\ K$ is the thermodynamic temperature in Kelvin, $R_L = 50\ K\Omega$ is the load resistance of the TIA, and $B = 1\ MHz$ is the bandwidth [38]. Then, the SNR can be defined as

$$SNR = \frac{(I_sM)^2}{\sigma_{shot}^2 + \sigma_{dark}^2 + \sigma_{themal}^2}$$
$$= \frac{(I_sM)^2}{2q(I_s+I_b+I_{self}+MI_{db})MF(M)B + 2qI_{ds}B + \frac{4KTB}{R_L}} \quad (21)$$

For a given photocurrent I_s, there is an optimal APD avalanche multiplication factor M_P that produces a maximum SNR. This value can be obtained when the first term in the denominator of the SNR equation (21) is equal to the second [39]. If we ignore the I_{ds} current, we obtain

$$F(M) = \frac{4K_BT}{2q(I_s + I_b + I_{self} + MI_{db})MR_L}$$
$$= \frac{1.035 \times 10^{-6}}{(I_s + I_b + I_{self} + MI_{db})M} = Q(I, M) \quad (22)$$

$$Q(I, M) = \frac{1.035 \times 10^{-6}}{(I_s + I_b + I_{self} + MI_{db})M}$$
$$= \frac{1.035 \times 10^{-6}}{(I + MI_{db})M}, I = I_s + I_b + I_{self} \quad (23)$$

The excess noise factor $F(M)$ is given by McIntyre's equation. It is given as

$$F(M, k) = M\left[1 - (1 - k)\left(\frac{M - 1}{M}\right)^2\right]$$
$$\approx kM + (1 - k)\left(2 - \frac{1}{M}\right) \approx M^x \quad (24)$$

where k is the ionization-coefficient ratio and x is the excess noise index. According to the APD data sheets, when M is 50, x is 0.2, and then $F(M)$ is 2.19. From these values, we can
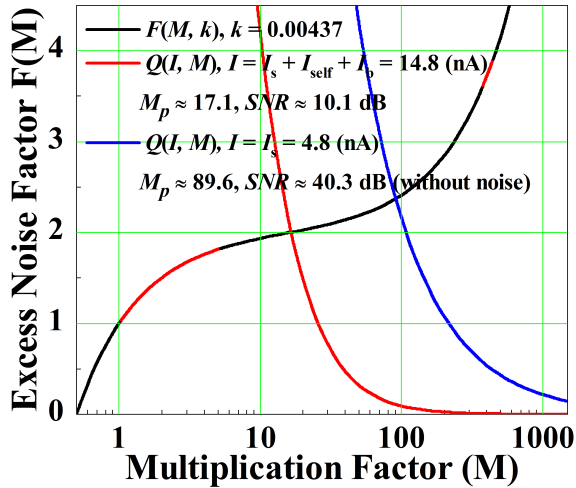
FIGURE 25. The optimal avalanche multiplication factor M_P at different APD received photocurrents.

FIGURE 27. The average photocurrent caused by self-interference and background noise $I_{self} + I_b \approx 10\ nA$.

TABLE 8. The APD relevant parameters with and without self-interference and background noise.

Photocurrent I	Multiplication facter M_P	APD reverse voltage V_R	SNR
14.8 nA	17.1	310 V	10.1 dB
4.8 nA	89.6	360 V	40.3 dB (no noise)

calculate $k = 0.00437$. Therefore, the $F(M)$ curve can be determined.

Fig. 25 shows the $F(M)$ and $Q(I, M)$ at $I = I_s + I_{self} + I_b$ and $I = I_s$ without self-interference and background noise. When I takes different values, the focus of curves $F(M)$ and $Q(I, M)$ corresponds to the optimal multiplication factor M_P. According to the functional relationship between M and the reverse voltage V_R in the APD data sheets, V_R can be determined. Here, I and $I_{self} + I_b$ can be obtained from Fig. 26 and Fig. 27, respectively.

$$I, I_{self} + I_b = \frac{q\eta_{qe}P_{R-opt}}{h\nu} = \frac{V(t)}{MR_L} \quad (25)$$
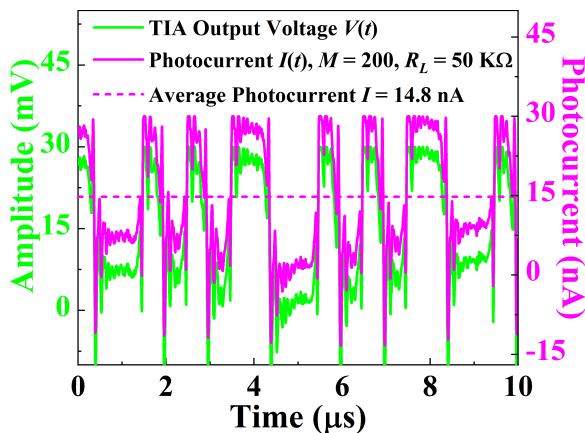

FIGURE 26. The average photocurrent $I = I_s + I_b + I_{self} \approx 14.8\ nA$.

Here, h is Planck's constant, ν is the optical frequency, η_{qe} is the quantum efficiency, $V(t)$ is the TIA output voltage, and P_{R-opt} is the received optical power of the APD. As shown in Fig. 25 and Table 8, the optimal multiplication factors M_P with and without self-interference and background noise are 17.1 and 89.6, and the values of V_R are
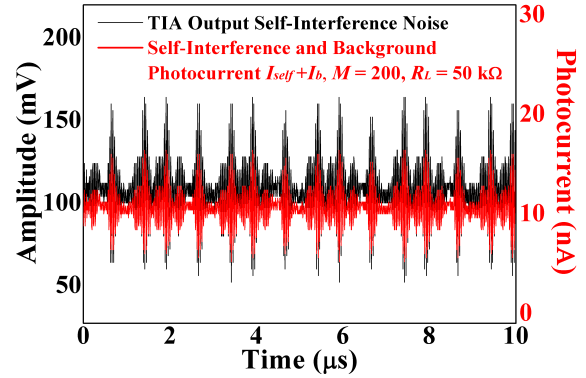
approximately 310 V and 360 V, respectively. The above analysis indicates that as the total photocurrent I increases, the value of M_P will decrease, resulting in a decrease in the optimal reverse voltage V_R of the APD. This means that self-interference and background noise will reduce the optimal bias voltage V_R of the APD. The SNR with and without self-interference and background noise can be calculated as

$$SNR = \frac{(I_s M)^2}{\sigma_{noise}^2} = \frac{(I_s M)^2}{\sigma_{shot}^2 + \sigma_{dark}^2 + \sigma_{themal}^2}$$
$$\approx \frac{6.74 \times 10^{-18}}{6.59 \times 10^{-19}} \approx 10.1\ dB, \quad M = 17.1,\ F(M) = 1.88 \quad (26)$$

$$SNR = \frac{(I_s M)^2}{\sigma_{noise}^2} = \frac{(I_s M)^2}{\sigma_{shot}^2 + \sigma_{dark}^2 + \sigma_{themal}^2}$$
$$\approx \frac{1.85 \times 10^{-13}}{6.82 \times 10^{-18}} \approx 40.3\ dB, \quad M = 89.6,\ F(M) = 2.4 \quad (27)$$

The above calculation results show that the SNR is seriously deteriorated due to the presence of self-interference and background noise. The corresponding results are listed in Table 9. If the system uses 2FSK coherent demodulation, the total error rate can be estimated as

$$P_e = \frac{1}{2}erfc\left(\sqrt{\frac{SNR}{2}}\right) \approx 7.3 \times 10^{-4} \quad (28)$$

$$erfc(x) = \frac{2}{\sqrt{\pi}} \int_x^\infty \exp\left(-t^2\right)dt \quad (29)$$

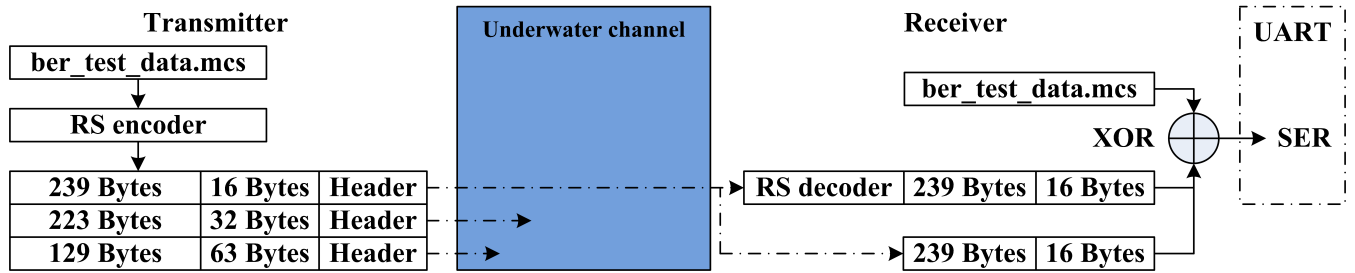where erfc(x) is the complementary error function and SNR is 10.01 dB.

FIGURE 28. The symbol error rate test method.

TABLE 9. Some parameters and corresponding results.

Symbol	Parameters	Value
d	optical link range	10 m
I_s	photocurrent	4.8 nA
$I_{self} + I_b$	self-interference photocurrent	10 nA
I_{db}	average bulk leakage current	1 nA
I	total photocurrent	14.8 nA
B	bandwidth	1 MHz
M_p	optimal avalanche multiplication	17.1
$F(M_p)$	excess noise factor	1.88
R_L	the load resistance of TIA	50 KΩ
SNR	signal-to-noise ratio	10.1 dB
SNR	no self-interference noise SNR	40.3 dB
V_R	reverse voltage of APD	310 V

As shown in the Fig. 28, we propose a simple method for testing the symbol error rate (SER). At the transmitter, the source data (known to the receiver) in the.mcs file is coded by RS (n, k) schemes and form a transmitted packet with the frame header (7CE3). The receiver starts decoding after receiving the corresponding frame header and finally outputs the received code stream (255 bytes) at 115200 Baud on the serial port. Then, the SER of the physical layer link after decoding and the SER without decoding are output, as shown in Table 10. When the video signal can be received normally and smoothly, the SER is very low.

TABLE 10. SER at different RS code schemes.

RS (n, k)	Physical layer SER	SER after RS decoding
RS (255, 239)	3.6×10^{-3}	3.9×10^{-6}
RS (255, 223)	2.9×10^{-3}	3.9×10^{-6}
RS (255, 129)	9.8×10^{-4}	3.9×10^{-6}

F. LINK DISTANCE EXTENSION AND PREDICTION

The reachable link distance of this system is limited by a tank with a fixed length of 10 m. If the optical power is increased, the link distance will be further extended. As shown in Fig. 29, the Beer-Lambert law is applied to predict the link extension distance from 10 m. The result is expressed in terms of decibels relative to one milliwatt (dBm) of power loss and is given as

$$(dBm)_{loss} = 10 \lg \left[\exp(-cd) \right] \approx -4.34 \, (cd) \qquad (30)$$
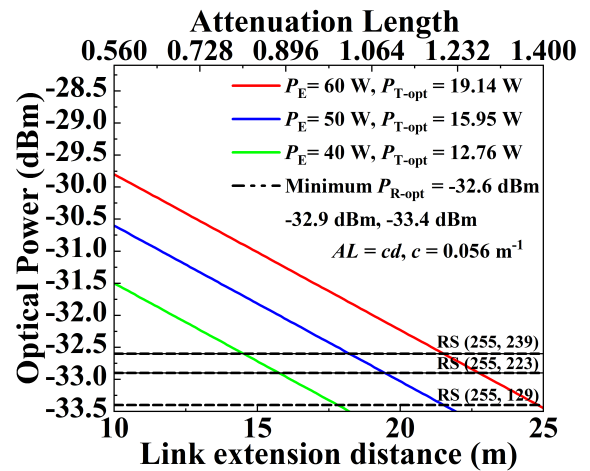

FIGURE 29. Link distance prediction using the Beer-Lambert law.

TABLE 11. Increase the link distance by reducing the half-power angle of the LED at RS (255, 239).

Optical power @ 10 m	Minimum received optical power	MATLAB simulation	Half-power angle of LED
-29.8 dBm	-32.6 dBm	21.5 m	3.47°
-30.6 dBm	-32.6 dBm	18.2 m	4.11°
-31.6 dBm	-32.6 dBm	14.5 m	5.12°
-32.6 dBm	-32.6 dBm	10.0 m	7.50°

where c is the attenuation coefficient and d is the link distance. To compare other water types, the corresponding attenuation length (AL) is also shown on the upper x axis in Fig. 29 and is given by [40]

$$AL = cd \qquad (31)$$

The disadvantage of the Beer-Lambert law is that the influence of the geometric attenuation of the optical source is ignored and the predicted link distance is overestimated. To assess such a link distance, the effect of geometric attenuation can be reduced by reducing the half-power angle of the LED. Table 11 shows the specific data obtained through MATLAB link simulations. At the same time, we use MATLAB simulations to consider the effects of both geometric and channel attenuation and predict the link length, as shown in Table 12. In theory, when the optical power

TABLE 12. Link distance prediction base on MATLAB simulations.

Electric power	Optical power	MATLAB simulation c = 0.056 /m	Attenuation length
60 W	19.14 W	14.5 m	0.80
50 W	15.95 W	13.1 m	0.73
40 W	12.76 W	11.5 m	0.64
31.6 W	10.07 W	10.0 m	0.56

TABLE 13. Cost analysis of the total UWOC system.

Items	Cost (USD)	Total (USD)
FPGA board × 2	600	
LED and driver board × 2	300	
APD and receiver board × 2	1,100	
lens design × 2	2,000	22,100
power supply board × 2	100	
mechanical structure × 2	3,000	
water tank × 1	15,000	

reaches a maximum of 19.14 W and the attenuation coefficient is 0.056 m^{-1}, the link distance can reach 14.5 m at RS (255, 239). Finally, the system cost analysis is shown in the Table 13.

IV. CONCLUSION

The development of novel UWOC systems is essential for meeting the growing demands of high-tech ocean research and for the exploitation of marine natural resources. In this work, we experimentally provided a real-time, full-duplex UWOC transmission system tested in an indoor water tank channel. Emphasis was placed on the system hardware structure, which was based on an FPGA and an underwater channel optical link model. We proposed an accurate method for calculating the electrical power consumption and transmitted optical power of a high-power LED array. A method for selecting a reasonable APD responsibility was also introduced. Specifically, we proposed a theoretical method for selecting the optimal reverse voltage of the APD to maximize the SNR. The system achieved 10 m underwater video transmission at a data rate of 1 Mbps. Duplex system applications are more diverse, but due to the phenomenon of self-interference, the transmission distance is relatively short. By increasing the transmitted optical power of the LED array, the theoretical maximum link distance can reach 14.5 m with an attenuation coefficient of 0.056 /m based on MATLAB simulations.

REFERENCES

[1] H. Kaushal and G. Kaddoum, "Underwater optical wireless communication," *IEEE Access*, vol. 4, pp. 1518–1547, 2016.

[2] Z. Zeng, S. Fu, H. Zhang, Y. Dong, and J. Cheng, "A survey of underwater optical wireless communications," *IEEE Commun. Surveys Tuts.*, vol. 19, no. 1, pp. 204–238, 1st Quart., 2017.

[3] H. M. Oubei, C. Shen, A. Kammoun, E. Zedini, K. Park, X. Sun, G. Liu, C. Kang, T. Ng, M.-S. Alouini, and B. S. Ooi, "Light based underwater wireless communications," *Jpn. J. Appl. Phys.*, vol. 57, no. 8, Jul. 2018, Art. no. 08PA06.

[4] J. Xu, "Underwater wireless optical communication: Why, what, and how?" *Chin. Opt. Lett.*, vol. 17, no. 10, pp. 1–10, Oct. 2019.

[5] J. Wang, C. Lu, S. Li, and Z. Xu, "100 m/500 Mbps underwater optical wireless communication using an NRZ-OOK modulated 520 nm laser diode," *Opt. Express*, vol. 27, no. 9, pp. 12171–12181, Apr. 2019.

[6] Y. Zhou, X. Zhu, F. Hu, J. Shi, F. Wang, P. Zou, J. Liu, F. Jiang, and N. Chi, "Common-anode LED on a Si substrate for beyond 15 Gbit/s underwater visible light communication," *Photon. Res.*, vol. 7, no. 9, pp. 1019–1028, Sep. 2019.

[7] H. M. Oubei, J. R. Duran, B. Janjua, H. Y. Wang, C. T. Tsai, Y. C. Chi, T. K. Ng, H. C. Kuo, J. H. He, M. S. Alouini, G. R. Lin, and B. S. Ooi, "4.8 Gbits/s 16-QAM-OFDM transmission based on compact 450-nm laser for underwater wireless optical communication," *Opt. Express*, vol. 23, no. 18, pp. 23302–23309, Sep. 2015.

[8] Y. Chen, M. Kong, T. Ali, J. Wang, R. Sarwar, J. Han, C. Guo, B. Sun, N. Deng, and J. Xu, "26 m/5.5 Gbps air-water optical wireless communication based on an OFDM-modulated 520-nm laser diode," *Opt. Express*, vol. 25, no. 13, pp. 14760–14765, Jun. 2017.

[9] X. Liu, S. Yi, X. Zhou, Z. Fang, Z. J. Qiu, L. Hu, C. Cong, L. Zheng, R. Liu, and P. Tian, "34.5m underwater optical wireless communication with 2.70 Gbps data rate based on a green laser diode with NRZ-OOK modulation," *Opt. Express*, vol. 25, no. 22, pp. 27937–27947, Oct. 2017.

[10] M. Doniec, A. Xu, and D. Rus, "Robust real-time underwater digital video streaming using optical communication," in *Proc. IEEE Int. Conf. Robot. Autom.*, Karlsruhe, Germany, May 2013, pp. 5117–5124.

[11] P. Wang, C. Li, and Z. Xu, "A cost-efficient real-time 25 Mb/s system for LED-UOWC: Design, channel coding, FPGA implementation, and characterization," *J. Lightw. Technol.*, vol. 36, no. 13, pp. 2627–2637, Jul. 1, 2018.

[12] J. Wang, C. Tian, X. Yang, W. Shi, Q. Niu, and T. A. Gulliver, "Underwater wireless optical communication system using a 16-QAM modulated 450-nm laser diode based on an FPGA," *Appl. Opt.*, vol. 58, no. 16, pp. 4553–4559, Jun. 2019.

[13] A. Al-Halafi, H. M. Oubei, B. S. Ooi, and B. Shihada, "Real-time video transmission over different underwater wireless optical channels using a directly modulated 520nm laser diode," *J. Opt. Commun. Netw.*, vol. 9, no. 10, pp. 826–832, Oct. 2017.

[14] M. Doniec, C. Detweiler, I. Vasilescu, M. Chitre, M. Hoffmann-Kuhnt, and D. Rus, "AquaOptical: A lightweight device for high-rate long-range underwater point-to-point communication," in *Proc. OCEANS*, Biloxi, MS, USA, Oct. 2009, pp. 1–6.

[15] M. W. Doniec and D. Rus, "Bidirectional optical communication with AquaOptical II," in *Proc. IEEE Int. Conf. Commun. Syst. (ICCS)*, Singapore, Dec. 2010, pp. 390–394.

[16] (2012). *Ambalux*. [Online]. Available: http://www.ambalux.com

[17] T. Sawa. *Study of Adaptive Underwater Optical Wireless Communication With Photomultiplier Tube.* Accessed: Jul. 26, 2017. [Online]. Available: http://www.godac.jamstec.go.jp/catalog/data

[18] S. Fasham and S. Dunn. *Bluecomm Underwater Optical Communications*. UK. [Online]. Available: http://www.sonardyne.com/products/all-products/instruments/1148-bluecomm-underwater-optical-modem.html

[19] W. Cox, "A 1 Mbps underwater communication system using a 405 nm laser diode and photomultiplier tube," M.S. thesis, Dept. Elect. Eng., North Carolina State Univ., Raleigh, NC, USA, 2008.

[20] W. C. Cox, J. A. Simpson, and J. F. Muth, "Underwater optical communication using software defined radio over LED and laser based links," in *Proc. Mil. Commun. Conf. (MILCOM)*, Nov. 2011, pp. 2057–2062.

[21] L. M. R. Brooks, "Musical toothbrush with adjustable neck and mirror," NEXIS Library, Patent D 326 189, May 19, 1992.

[22] Y. Li, H. Yin, X. Ji, and B. Wu, "Design and implementation of underwater wireless optical communication system with high-speed and full-duplex using Blue/Green light," in *Proc. 10th Int. Conf. Commun. Softw. Netw. (ICCSN)*, Chengdu, China, Jul. 2018, pp. 99–103.

[23] Z. Wei, X. Mu, and H. Fu, "Wearable full-duplex digital transceiver for underwater optical wireless communications," in *Proc. Pacific Rim Conf. (CLEO)*, Hong Kong, 2018, pp. 1–2.

[24] B. Han, W. Zhao, J. Meng, Y. Zheng, and Q. Yang, "Study on the backscattering disturbance in duplex underwater wireless optical communication systems," *Appl. Opt.*, vol. 57, no. 29, pp. 8478–8486, Oct. 2018.

[25] J. Everett, "Forward-error correction coding for underwater free-space optical communication," M.S. thesis, Dept. Elect. Eng., North Carolina State Univ., Raleigh, NC, USA, 2009.

[26] W. C. Cox, J. A. Simpson, C. P. Domizioli, J. F. Muth, and B. L. Hughes, "An underwater optical communication system implementing Reed–Solomon channel coding," in *Proc. OCEANS*, Quebec City, QC, Canada, 2008, pp. 1–6.

[27] D. Madhuri and P. C. Reddy, "Performance comparison of TCP, UDP and SCTP in a wired network," in *Proc. Int. Conf. Commun. Electron. Syst. (ICCES)*, Oct. 2016, pp. 1–6.

[28] R. M. Hagem, D. V. Thiel, S. G. O'Keefe, A. Wixted, and T. Fickenscher, "Low-cost short -range wireless optical FSK modem for swimmers feedback," in *Proc. IEEE SENSORS*, Oct. 2011, pp. 258–261.

[29] M. Kong, Y. Chen, R. Sarwar, B. Sun, Z. Xu, J. Han, J. Chen, H. Qin, and J. Xu, "Underwater wireless optical communication using an arrayed transmitter/receiver and optical superimposition-based PAM-4 signal," *Opt. Express*, vol. 26, no. 3, pp. 3087–3097, Feb. 2018.

[30] Y. Chen, S. Wen, Y. Wu, Y. Ren, W. Guan, and Y. Zhou, "Long-range visible light communication system based on LED collimating lens," *Opt. Commun.*, vol. 377, pp. 83–88, Oct. 2016.

[31] C. D. Mobley, *Light and Water: Radiative Transfer in Natural Waters*. San Diego, CA, USA: Academic, 1994.

[32] M. Doniec, M. Angermann, and D. Rus, "An end-to-end signal strength model for underwater optical communications," *IEEE J. Ocean. Eng.*, vol. 38, no. 4, pp. 743–757, Oct. 2013.

[33] S. Tang, Y. Dong, and X. Zhang, "On path loss of NLOS underwater wireless optical communication links," in *Proc. MTS/IEEE OCEANS Bergen*, Bergen, Norway, Jun. 2013, pp. 1–3.

[34] T. Komine and M. Nakagawa, "Fundamental analysis for visible-light communication system using LED lights," *IEEE Trans. Consum. Electron.*, vol. 50, no. 1, pp. 100–107, Feb. 2004.

[35] P. H. Pathak, X. Feng, P. Hu, and P. Mohapatra, "Visible light communication, networking, and sensing: A survey, potential and challenges," *IEEE Commun. Surveys Tuts.*, vol. 17, no. 4, pp. 2047–2077, Nov. 2015.

[36] C. Gabriel, M.-A. Khalighi, S. Bourennane, P. Leon, and V. Rigaud, "Monte-Carlo-based channel characterization for underwater optical communication systems," *IEEE/OSA J. Opt. Commun. Netw.*, vol. 5, no. 1, pp. 1–12, Jan. 2013.

[37] Z. Ghassemlooy, W. Popoola, and S. Rajbhandari, *Optical Wireless Communications: System and Channel Modelling With MATLAB*, 1th ed. New York, NY, USA: CRC Press, 2013.

[38] F. Xu, M. A. Khalighi, and S. Bourennane, "Impact of different noise sources on the performance of PIN-and APD-based FSO receivers," in *Proc. 11th Int. Conf. Telecommu.*, Graz, Austria, Jul. 2011, pp. 211–218.

[39] S. M. Sze, *Semiconductor Devices: Physics and Technology*. New York, NY, USA: Wiley, 1985.

[40] W. Cox and J. Muth, "Simulating channel losses in an underwater optical communication system," *J. Opt. Soc. Amer. A, Opt. Image Sci.*, vol. 31, no. 5, pp. 920–934, May 2014.
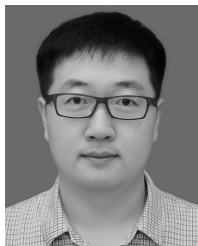
JINJIA LI (Member, IEEE) was born in Qiqihar, Heilongjiang, China, in 1982. He received the B.S. and M.S. degrees in electronic and information engineering, signal and information processing from the Harbin University of Science and Technology (HUST), Heilongjiang, China, in 2006 and 2012, respectively. He is currently pursuing the Ph.D. degree in communication and information system with the Peter Grünberg Research Center, Nanjing University of Posts and Telecommunications (NJUPT), Jiangsu, China.

From 2006 to 2008, he was a Hardware Engineer with Precision Electronics Company Ltd. Since 2012, he has been a Lecturer with the College of Rongcheng, HUST. He is the author of one book and more than five journal or conference articles. His current research interests include underwater wireless optical communication (UWOC) and visible light communication (VLC) technology.

Mr. Li was a Member of OSA. He received the Excellent Master Student from the Harbin University of Science and Technology.

BO YANG (Member, IEEE) was born in Nanyang, Henan, China, in 1980. He received the B.S. degree from Zhengzhou University, in 2001, and the M.S. degree from Xidian University, in 2005. He is currently pursuing the Ph.D. degree in communication and information system with the Nanjing University of Posts and Telecommunications, Jiangsu, China.

He joined ZTE Cooperation, in 2005. He has been with the Nanjing Researching Center engaged in research of 3G/4G mobile network, since 2013. After 2013, he joined the National RFID Production Quality Supervision and Testing Center in electromagnetic compatibility researching, China. He studied the near field magnetic imaging using NV center in diamond, in 2016. He began to develop underwater wireless optical communication system, in 2017. He is currently responsible for technical support of several international projects, such as H3G Austria and Deutsche Telekom, German. His main research interests include wireless optical communication and quantum magnetic field imaging.

DEMAO YE was born in 1982. He received the Ph.D. degree from Wuhan University, in June 2009.

He is currently a Professor with the 713th Research Institute, China Shipbuilding Industry Corporation (CSIC), Zhengzhou, China. He has published 18 articles. He holds over 14 invention patents. His research interests include ultrahigh-precision tracking, high-speed image processing, and underwater wireless optical communication. He received the Second Prize of Science and Technology Progress Award of CSIC (ranking First), the Third Prize from the National Defense Science and Technology Progress Award (ranking First), and the Winning Award from the Second China Civil and Military Technology Innovation and Application Competition (ranking First).

LINNING WANG received the B.S. degree in communication engineering from the Nanjing University of Posts and Telecommunications, Jiangsu, China, in 2018. He is currently pursuing the master's degree in electronics and communication engineering with the Nanjing University of Posts and Telecommunications.

He has organized and completed undergraduate innovation and entrepreneurship projects. He has strong coordination and communication skills and the ability to organize and solve problems. During one year, he completed the realization and improvement of some functions of visible light audio transmission systems, underwater visible light communication systems, and has submitted a patent.
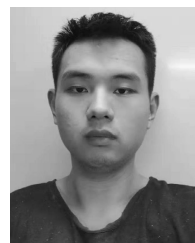
KANG FU received the B.S. degree in electronic information science and technology from the Nanjing University of Posts and Telecommunications, Jiangsu, China, in 2018, where he is currently pursuing the M.S. degree in communication and information system with the Peter Grünberg Research Center.

From 2014 to 2018, he was an Outstanding Cadre with the Student Union of the School and the Vice-Head of the Class. He has participated with the Electronic Design Project of Junior High School and achieved Excellent Results. His research interest includes underwater wireless optical communication.

Mr. Fu Team received the Second Prize from the Graduate Electronic Design Competition, East China, in 2019.

JINLONG PIAO received the M.S. degree in electronic and communications engineering from Henan Normal University, in 2018. He is currently pursuing the Ph.D. degree in communication and information system with the Peter Grünberg Research Center, Nanjing University of Posts and Telecommunications, Jiangsu, China.

From 2015 to 2018, he engaged research of earthquake prediction model using VLF signal propagation method. His current research interests include monolithic intergration GaN LED and MOSFET devices based on silicon, vertical-structure LEDs, and visible light communications.

YONGJIN WANG received the Ph.D. degree in micro-electronics and solid-state electronics from the Shanghai Institute of Microsystem and Information Technology, Chinese Academy of Sciences (CAS), in 2005.

He involved in research work with the University of Freiburg, Germany, Tohoku University, Germany, Forschungszentrum, Jülich, and the University of Bristol. Since 2011, he has been a Professor and a Ph.D. Tutor with the Nanjing University of Posts and Telecommunications. His current research interests include visible light communications, III-nitride monolithic circuit, and sub-wavelength vertical-structure LEDs. He was a recipient of numerous scholarships, which include the Humboldt Foundation Scholarship, the JSPS Special Researcher Scholarship, and the Royal Society or Engineering Scholarship. He received the National Science Fund for Outstanding Youth, in 2013.

○ ○ ○